THE JOURNAL OF PHYSICAL CHEMISTRY C

Article

Cite This: J. Phys. Chem. C 2018, 122, 5992−6004

pubs.acs.org/JPCC

Nanoscale Chemical Degradation Mechanisms of Sulfate Attack in Alkali-activated Slag

Kai Gong[†,‡] and Claire E. White*[,†,‡]

[†]Department of Civil and Environmental Engineering and [‡]the Andlinger Center for Energy and the Environment, Princeton University, Princeton, New Jersey 08544, United States

Supporting Information

ABSTRACT: Chemically induced material degradation is a major durability issue facing many technologically important materials systems, including conventional and new sustainable cementitious materials. In this study, the nanoscale chemical degradation mechanisms have been elucidated for an amorphous sodium hydroxide-activated slag paste (one type of sustainable cement) exposed to different types of sulfate-bearing solutions (i.e., Na_2SO_4, $MgSO_4$, and H_2SO_4), by combining synchrotron-based X-ray diffraction (XRD), Fourier transform infrared (FTIR) spectroscopy and X-ray pair distribution function (PDF) analysis. The XRD, FTIR, and PDF results show that the chemistry and structure of the paste is essentially immune to Na_2SO_4 attack, whereas exposure to 5−10 wt % $MgSO_4$ and H_2SO_4 cause complete disintegration of the main binder gel (i.e., sodium-containing calcium−(alumino)−silicate−hydrate), along with formation of magnesium−silicate−hydrate or silica-rich gels and extensive precipitation of gypsum. These differences appear to be directly correlated with the ability of the ions (i.e., Na^+, Mg^{2+}, H^+) accompanying SO_4^{2-} to alter the pH of the pore solution in the samples. By correlating the changes that occurred to the phase composition and the structure of the paste with the pH data from the equilibrated solutions, this study has provided important mechanistic insight on the fundamental sulfate-induced degradation reactions occurring in hydroxide-activated slag.

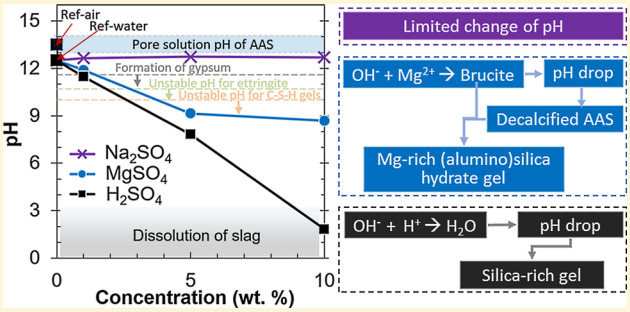

1. INTRODUCTION

Alkali-activated materials (AAMs), including alkali-activated slags (AASs) and those classified as geopolymers, are a class of low-CO_2 cements that are being actively pursued as alternatives for ordinary Portland cement (OPC) paste. The carbon footprint of the concrete construction industry contributes approximately 5−8% of anthropogenic CO_2 emissions due to extensive usage of OPC powder which must be manufactured from limestone and clays.[1−3] AAMs are synthesized by mixing an amorphous aluminosilicate source (denoted as precursor) with an alkaline activator, where the precursor particles dissolve and reprecipitate to form an interconnected gel network,[2] similar to the gel that forms during hydration of ordinary Portland cement (OPC)[4,5] (especially for high-calcium AAMs). This gel makes up the main binder phase in AAMs, and is primarily responsible for most engineering properties of the cement/concrete, similar to the role of calcium−silicate−hydrate (C−S−H) gel in OPC-based systems. Numerous studies have shown that AAMs exhibit similar mechanical properties compared with OPC-based systems when properly formulated.[6] However, questions still remain regarding their long-term durability performance under different environmental conditions relevant to building and infrastructure materials, primarily due to the lack of an extensive long-term track record. This missing information on the long-term durability performance is considered a major obstacle impeding large-scale adoption of AAMs in the construction industry.[7]

One durability issue facing AAMs is sulfate attack induced by reactions with sulfate-bearing chemicals (e.g., Na_2SO_4, $MgSO_4$, and H_2SO_4), which are ubiquitous in many building environments.[7−9] For OPC-based concrete, sulfate attack occurs when sulfate ions permeate through the pore network and react with calcium and aluminum phases in the OPC paste to form expansive ettringite and/or gypsum.[10−14] The formation of these phases, ettringite in particular, leads to a buildup of crystallization pressure that can cause expansion and cracking of the concrete.[15,16] The cracking of concrete provides an easier path for the ingress of additional sulfate ions and other aggressive chemicals, which not only accelerates the rate of sulfate attack but also increases the corrosion risk of the embedded steel rebar (if present). Since there are readily available sources of calcium (i.e., portlandite ($Ca(OH)_2$) and aluminum (i.e., monosulfoaluminate ($Ca_4Al_2(OH)_{12}\cdot SO_4\cdot 6H_2O$)) in OPC paste, sulfate ions preferably react with these phases when they are present, which delays attack of the main binder phase, C−S−H gel.[11,12,17] This degradation

Received: November 14, 2017
Revised: January 31, 2018
Published: February 28, 2018

DOI: 10.1021/acs.jpcc.7b11270
J. Phys. Chem. C 2018, 122, 5992−6004

mechanism is different from AAM-based material systems which do not contain any portlandite or monosulfoaluminate phases. For the case of AAMs, sulfate attack may directly target the main binding gels, such as sodium-containing aluminum-substituted calcium−silicate−hydrate (C−(N)−A−S−H) gel in AAS, as has been reported for blended OPC cements containing slag and silica-fume where portlandite is depleted due to pozzolanic reaction with the slag and silica fume.[13,18]

AAS is typically made by alkaline activation of blast furnace slag, a highly amorphous aluminosilicate glass charge balanced by Ca and Mg. Because of the high Ca content of slag, the principle reaction product in AAS is a C−(N)−A−S−H gel with a chain-like structure (the aluminosilicate chains are mostly Q^1 and Q^2),[19−22] similar to the C−S−H gel in OPC-based systems.[23] This C−(N)−A−S−H gel in AAS is very different from low-Ca AAMs (e.g., metakaolin-based or class F fly ash-based AAMs), where the reaction product is an amorphous and highly polymerized aluminosilicate gel (predominately Q^4) charge balanced by Na, which is generally known as N−A−S−(H) gel.[2] The main difference between C−(N)−A−S−H in AAS and C−S−H in OPC is (1) the presence of a small amount of Q^3 in C−(N)−A−S−H, (2) a lower Ca/Si ratio in C−(N)−A−S−H compared with C−S−H due to the lower Ca content of the precursor (slag versus OPC powder), (3) substitution of Al into tetrahedral bridging silica sites in C−(N)−A−S−H, and (4) the presence of alkalis (i.e., Na).[19,21,22] In addition to the C−(N)−A−S−H gel, a secondary phase such as a hydrotalcite-like layered double hydroxide (LDH) is often observed in AAS paste.[24−26] Because of the absence of portlandite and monosulfoaluminate in AAS, the C−(N)−A−S−H gel may be directly targeted during sulfate attack.

Although many studies have investigated sulfate-induced degradation of AAS,[8,9,17,27−30] there are outstanding questions regarding the chemical degradation mechanisms occurring in AAS due to sulfate attack. To date, most studies have focused on macroscopic measurements such as mechanical strength, weight loss, expansion and corrosion depth,[8,9,17,27−29] with only a few investigations[17,28,30] reporting the impact of sulfate attack on the chemical phases in AAS. Ismail et al.[30] studied alkali-activated fly ash/slag pastes that were exposed to 5 wt % $MgSO_4$ and Na_2SO_4 solutions for 3 months and observed extensive physical deterioration in the pastes exposed to $MgSO_4$ but not those exposed to Na_2SO_4. Fourier transform infrared (FTIR) spectroscopy and X-ray diffraction (XRD) results revealed that exposure to 5 wt % $MgSO_4$ led to a higher degree of polymerization of the C−(N)−A−S−H gel along with extensive formation of gypsum, which was not observed for the Na_2SO_4-exposed samples. Hence, the effect of Na_2SO_4 exposure on AAS is very different from its effect on OPC-based materials, where previous investigations have shown that expansive ettringite and sometimes gypsum formed, which led to significant macroscopic expansion and cracking of the OPC-based samples,[8,10−12,14] via crystallization pressure effects.[16] This difference may be attributed to the fact that there are readily accessible sources of Ca and Al in OPC-based materials for the formation of ettringite and gypsum, which are not as easily accessible in AAS.[17] Nevertheless, it has been reported that exposure to a periodically renewed 5 wt % Na_2SO_4 solution for 12 months led to a reduction in compressive strength (up to ∼17%) of an AAS-based concrete.[17]

For AAS exposed to $MgSO_4$ solutions, scanning electron microscope combined with energy dispersive X-ray spectroscopy (SEM−EDX) analysis[7,30] showed that there was a significant decrease in the Ca/Si ratio and an increase in the Mg/Si ratio for the binder as a result of exposure, which is consistent with SEM−EDX results on $MgSO_4$-exposed OPC samples.[14,31] It has been postulated that $MgSO_4$ attack leads to a transformation of the C−(N)−A−S−H and C−S−H gels to a magnesium−(alumino)silicate−hydrate (M−(A)−S−H) gel for AAS[7] and a magnesium-silicate-hydrate (M−S−H) gel for OPC-based materials,[14,31] which have lower cohesive strengths compared with C−(N)−A−S−H and C−S−H gels. These transformations, along with the formation of expansive gypsum, have been identified as the main factors responsible for the reported strength loss in both AAS[17] and OPC-based materials.[12] However, there is no direct experimental evidence for the formation of M−(A)−S−H/M−S−H in these systems, mainly due to the highly disordered nature of the C−(N)−A−S−H and M−(A)−S−H/M−S−H gels.

Studies have also shown that exposure to H_2SO_4 solutions causes severe degradation of AAS.[9,27,28,32,33] Recently, Aliques-Granero et al.[28] examined AAS pastes exposed to 1−5 wt % H_2SO_4 solutions for 28 days using XRD, where they observed the formation of gypsum and the loss of C−(N)−A−S−H gel in the attacked surface regions along with expansion of the samples. SEM−EDX analysis of the attacked regions revealed the presence of precipitated gypsum and a reduced Si and Al content indicating that these two elements partially dissolve during this type of sulfate attack. Previous SEM−EDX analysis on alkali-activated slag/fly ash pastes exposed to pH 1−3 H_2SO_4 solutions[32,33] showed the presence of many thin sublayers rich in Si and Al but depleted in Ca and Na in the attacked region, separated by gypsum precipitates. On the basis of these observations the authors[28,32,33] proposed a two-step degradation mechanism for H_2SO_4 attack of AAS samples: (1) ion exchange reaction between H_3O^+ in the solution and Ca^{2+} from C−(N)−A−S−H gel leading to decalcification of the C−(N)−A−S−H gel, and an electrophilic attack of the Si−O−Al bonds by H^+ resulting in formation of a siliceous gel structure (2) precipitation of gypsum after the leached Ca^{2+} reacts with SO_4^{2-} ions from the solution.

It is evident from the above studies that we do not fully understand the detailed chemical degradation mechanisms at play in AAS exposed to different sulfate-bearing chemicals. However, elucidating these chemical degradation mechanisms is particularly important for AAS (as well as other types of AAMs) because the chemical degradation processes involved in these systems are likely to differ from OPC-based systems due to their different chemistries, and hence the physical degradation mechanism identified for OPC-based systems (e.g., development of crystallization pressure effects via formation of ettringite and/or gypsum[15,16]) may also differ for AAMs. Therefore, this experimental study aims to elucidate and unify the chemical degradation mechanisms in AAS by analyzing the changes occurring to the chemistry and local atomic structure of a NaOH-activated slag paste exposed to different concentrations of Na_2SO_4, $MgSO_4$, and H_2SO_4 solutions. To minimize/eliminate the impact of ion diffusion through the pore network, the AAS samples have been crushed into fine powders prior to immersion in the different sulfate solutions. The use of powders allows the AAS particles to have full exposure to the sulfate-bearing chemicals and hence this approach significantly accelerates the sulfate attack process. X-ray pair distribution function (PDF) analysis is employed to assess the extent of change in the local atomic structure of the

DOI: 10.1021/acs.jpcc.7b11270
J. Phys. Chem. C 2018, 122, 5992−6004

Table 1. Chemical Composition of Neat Slag Obtained Using X-ray Fluorescence (XRF)[37]

oxide component	CaO	SiO_2	Al_2O_3	MgO	SO_3	other
weight percentage (%)	42.5	34.5	11.7	7.3	1.7	2.3

AAS powder due to immersion in the different sulfate solutions. PDF analysis is ideally suited for studying the local atomic structure of highly disordered materials and has been used extensively to investigate the structural changes occurring in amorphous/nanocrystalline material systems subjected to alkaline activation,[34−36] carbonation,[37,38] heating[39−42] and high pressure/mechanical stress.[43,44] Synchrotron-based XRD is used in this investigation to trace the sulfate-induced changes in the (nano)crystalline phases of the AAS paste. Furthermore, the impact of sulfate exposure on the extent of Si/Al polymerization associated with the main binder gel (i.e., C−(N)−A−S−H) in the AAS paste is examined using FTIR. Finally, the pH of the sulfate solutions before and after exposure has been monitored using an electronic pH meter, providing important information on the removal of hydroxyl ions from the AAS paste during sulfate attack.

2. MATERIALS AND METHODS

2.1. Materials and Sample Preparation. Ground granulated blast-furnace slag with a chemical composition shown in Table 1 was used in this investigation. The sodium hydroxide activating solution was prepared by dissolving NaOH pellets (Sigma−Aldrich, reagent grade) in distilled water. The slag was activated with this sodium hydroxide solution such that the mix proportions were 4 g of Na_2O and 50 g of H_2O for every 100 g of slag. The mixture (∼15 g) was initially hand mixed for 1 min and then subjected to vibration (using a vortex mixer) for 2 min to ensure homogeneous mixing. The mixture was then sealed in airtight containers (∼5 g per container) and cured at room temperature (20 °C) for 40 days, after which the samples were demolded and ground into a powder form using a mortar and pestle before being immersed in different types of sulfate solutions (i.e., Na_2SO_4, $MgSO_4$, and H_2SO_4) with different concentrations by weight (i.e., 1, 5 and 10%). Weight percentage (rather than molar concentration) was used to align with existing literature on sulfate attack.[9,16,17,28,31] For each immersed powder sample, ∼1 g of powder was added to ∼10 g of solution. The use of powder samples in this investigation allows for the chemical interactions between the samples and the sulfate-bearing chemicals to be studied independent of transport properties. This method not only simplifies data interpretation but also significantly accelerates the rate of sulfate attack, which usually takes months or even years using the standard testing methods developed for OPC-based systems.

Two reference samples were also prepared: one was immersed in distilled water (Ref−water) while the other was stored in a sealed container (Ref−air). The Ref−water data are presented in this article with the sulfate-exposed data, while the Ref−air data are given in the Supporting Information. After soaking in the solutions for 10 days, the samples were filtered, rinsed with distilled water, and mildly dried under a flow of N_2 gas. Samples were then loaded into polyimide capillaries (sealed with epoxy on both ends) for measurement on 11-ID-B at the Advanced Photon Source (APS) at Argonne National Laboratory (ANL). The remaining powders were stored in airtight containers for subsequent FTIR analysis.

2.2. Experimental Details. X-ray total scattering experiments were performed at room temperature using the 11-ID-B beamline at the APS. A wavelength of 0.2112 Å and a Perkin-Elmer amorphous silicon two-dimensional image plate detector[45] were used. The wavelength was selected to provide a compromise between high flux (statistics), Q-resolution and a sufficient maximum momentum transfer. The detector was located 180 mm from the sample. Data were collected for 2 min per sample. The data conversion from 2D to 1D was carried out using the program Fit2D[46,47] with CeO_2 as the calibration material. The PDF, $G(r)$, is obtained by taking a sine Fourier transform of the measured total scattering function, $S(Q)$, where Q is the momentum transfer, as outlined by Egami and Billinge.[48] The PDF data were obtained using PDFgetX2,[49] with a Q_{max} of 20 $Å^{-1}$. The instrument parameters were refined by using a standard calibration material (CeO_2) and the refinement program PDFgui.[50] The refined parameters (Q_{broad} = 0.010 $Å^{-1}$ and Q_{damp} = 0.034 $Å^{-1}$) were used for removal of crystalline phases during analysis of the PDF data.

Immediately after the X-ray total scattering experiment, XRD data were collected for 30 s for each sample on the 11-ID-B beamline at a sample−detector distance of 950 mm. Attenuated total reflectance (ATR)-FTIR measurements have also been performed on all samples using a Nicolet 730 FTIR instrument, purged with a N_2 flow. For each sample, 16 scans were collected from 4000 to 500 cm^{-1} with a resolution of 4 cm^{-1}. Moreover, the pH of the sulfate solutions prior to, and after immersion of the samples for 10 days has been measured using an electronic pH meter (Oakton 1100 Series Benchtop Meter) which was calibrated using three buffer solutions with pH values of 4, 7, and 10. Each pH measurement was taken after an equilibration period of 20 min.

3. RESULTS AND DISCUSSION

3.1. Impact of Sulfate Attack on Phase Stability in AAS Paste. The impact of exposure to different concentrations of Na_2SO_4, $MgSO_4$, and H_2SO_4 solutions on the stability of the chemical phases in the NaOH-activated slag paste has been evaluated using synchrotron-based XRD. The XRD patterns along with the phases identified in the samples are given in Figure 1, which clearly show that the phases present in the sulfate-exposed samples vary considerably depending on the type and concentration of the sulfate solution. For the Ref−water sample, the XRD pattern is dominated by two phases: a C−(N)−A−S−H gel phase with broad Bragg peaks matching those of the poorly crystalline C−S−H(I) ($CaO{\cdot}SiO_2{\cdot}HO$, PDF #00-034-0002) and a hydrotalcite-like LDH structure ($Mg_6Al_2(CO_3)(OH)_{16}{\cdot}4H_2O$, PDF #00-014-0191), which are the typical phases found in NaOH-activated slag pastes.[2,24−26,37] After exposure to Na_2SO_4 solutions, even at high concentrations (i.e., 5−10 wt %), the C−(N)−A−S−H gel and hydrotalcite-like phases are still present (Figure 1a), which suggests that these two phases are largely stable under Na_2SO_4 attack in a sealed environment. A major difference between the Ref−water sample and the Na_2SO_4-exposed samples is that ettringite ($Ca_6Al_2(SO_4)_3(OH)_{12}{\cdot}26H_2O$, PDF #01-073-6239) forms in the latter. Nevertheless, it is clear from the XRD patterns in Figure 1a that the amount of ettringite is

DOI: 10.1021/acs.jpcc.7b11270
J. Phys. Chem. C 2018, 122, 5992−6004

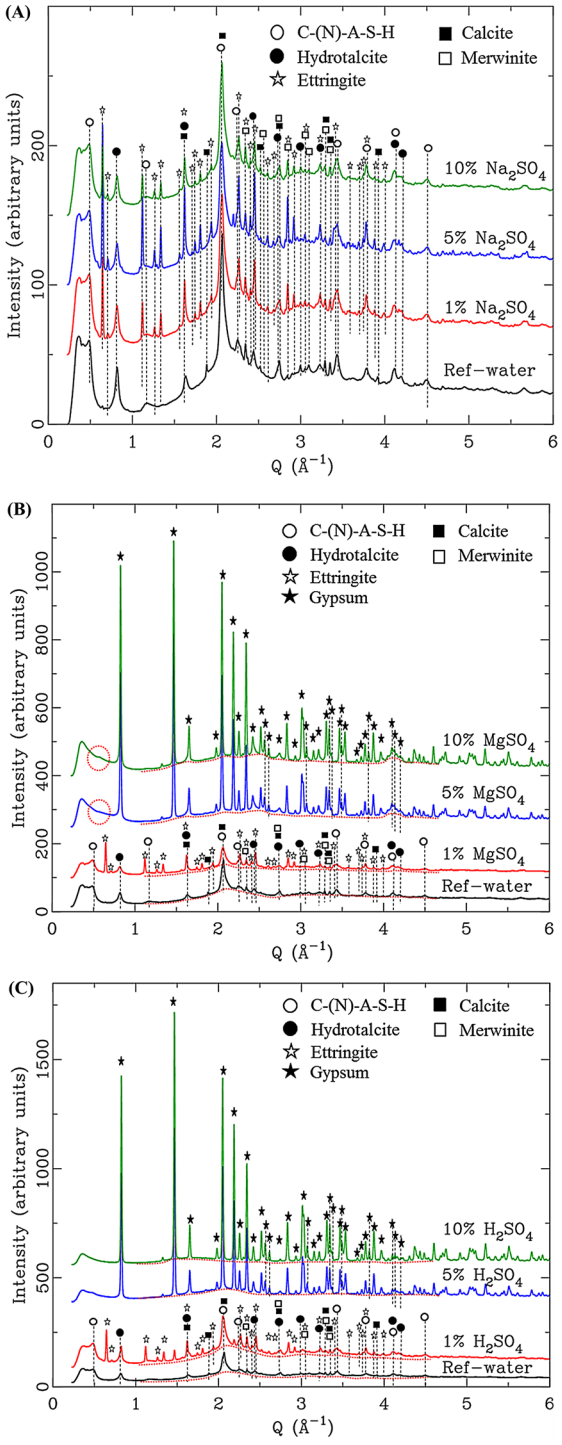

Figure 1. Stacked plot of the XRD patterns for the NaOH-activated slag paste that has been exposed to different concentrations of (a) Na_2SO_4, (b) $MgSO_4$, and (c) H_2SO_4 solutions. The broad diffuse peaks in parts b and c are highlighted using red dotted lines, and the diffuse shoulder at ~0.57 $Å^{-1}$ in part b is outlined by the red dotted circles.

relatively small, as further illustrated by the long-range X-ray PDF data in Figure S1 of the Supporting Information (no obvious increase in the long-range ordering was observed after Na_2SO_4 exposure). A broad diffuse peak located at a Q value of ~2.15 $Å^{-1}$ can be observed in all the XRD patterns in Figure 1a. This is consistent with the presence of unreacted slag[26] (refer to Figure S2a in Supporting Information for direct comparison), which is expected for NaOH-activated slag pastes that have cured for less than 2 months. It should be noted that the first peak at ~0.36 $Å^{-1}$, seen in all the XRD patterns in Figure 1, has not been assigned to any phase because this Q value overlaps with the small-angle scattering region and part of the scattered beam has been cut off by the beam stop.

In contrast to Na_2SO_4, exposure to $MgSO_4$ solutions, especially at higher concentrations (i.e., 5−10 wt %), significantly alters the phase composition of NaOH-activated slag paste, as illustrated in Figure 1b. In the 1 wt % $MgSO_4$-exposed sample, both the C−(N)−A−S−H gel and the hydrotalcite-like phase remain clearly visible along with formation of a small amount of ettringite, which is similar to the case of Na_2SO_4 exposure. However, at 5−10 wt % $MgSO_4$, extensive formation of gypsum is observed along with the disappearance of the C−(N)−A−S−H phase peaks (i.e., the peak at ~0.49 $Å^{-1}$ corresponding to the interlayer distance and the main peak at ~2.05 $Å^{-1}$), indicating a complete loss of the C−(N)−A−S−H gel in these two samples. The XRD peaks of the hydrotalcite-like phase overlap with those of gypsum, hence it is unclear whether the hydrotalcite-like phase dissolves based on these data. A closer examination of the XRD patterns for the 5−10 wt % $MgSO_4$-exposed samples reveals the emergence of two new broad diffuse peaks at ~2.47 and ~4.11 $Å^{-1}$ along with a shoulder at ~0.57 $Å^{-1}$, which may be indicative of a highly disordered M−(A)−S−H phase, such as disordered talc (refer to Figure S2a in the Supporting Information for direct comparison of the broad diffuse peaks).[51]

The XRD patterns of the NaOH-activated slag paste exposed to different concentrations of H_2SO_4 are given in Figure 1c. It is seen that H_2SO_4 exposure is even more aggressive than $MgSO_4$, especially via the significant amount of gypsum formed in the 5 and 10 wt % H_2SO_4-exposed samples. In the 1 wt % H_2SO_4-exposed sample, a small amount of gypsum is observed in addition to formation of ettringite. Nevertheless, there is still a strong presence of C−(N)−A−S−H gel and the hydrotalcite-like phase in this sample, indicating that these two phases are largely stable at 1 wt % H_2SO_4. On the other hand, for samples exposed to 5 and 10 wt % H_2SO_4, the C−(N)−A−S−H gel phase is completely lost. Furthermore, the broad diffuse peak at ~2.15 $Å^{-1}$ in the original paste, attributed to unreacted slag,[26] mostly disappears after immersion in 10 wt % H_2SO_4. This implies that the 10 wt % H_2SO_4 solution attacks both the binder gel and the unreacted slag. The dissolution of the unreacted slag in the sample exposed to 10 wt % H_2SO_4 is consistent with the literature,[52,53] which report slag dissolution in acidic conditions. Finally, for the 10 wt % H_2SO_4-exposed sample a broad diffuse peak at ~1.5−1.6 $Å^{-1}$ (corresponding to a 2θ value of ~21−23° for Cu radiation) emerges, which aligns well with the broad XRD peak (centered at a 2θ value of ~22°) for amorphous SiO_2 (refer to Figure S2b in the Supporting Information for direct comparison).[54]

The discrepancies in the phase compositions between the samples exposed to different sulfate solutions appear to be directly correlated with the equilibrated solution pH values after immersion of the NaOH-activated slag paste, as shown in Figure 2 (the detailed pH values are given in Table S1 in the Supporting Information). Although we have not directly measured the pH of the sample pore solution, the pH of the sulfate solutions after 10 days of sample immersion in a closed system (Figure 2) can be used to represent the pore solution pH since it is estimated that equilibrium has been reached within 10 days of exposure (calculation shown in the

DOI: 10.1021/acs.jpcc.7b11270
J. Phys. Chem. C 2018, 122, 5992−6004

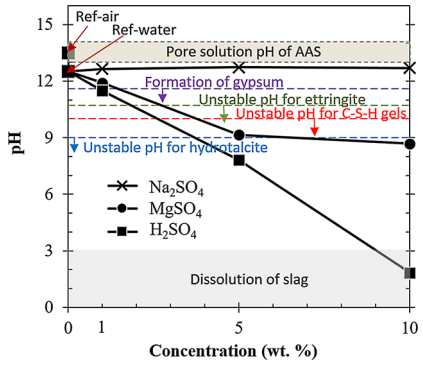

Figure 2. Solution pH of the immersed NaOH-activated slag paste samples (in different concentrations of Na_2SO_4, $MgSO_4$, and H_2SO_4 solutions) after 10 days of exposure. The pH of the pore solution given for "Ref–air" (~13–14, denoting unexposed sample) has been obtained from the literature for similar types of AASs.[62] The formation pH of gypsum (<~11.6),[61] and unstable pH range for ettringite (<~10.7),[60] C–S–H-type gels (<~10.0),[58] and hydrotalcite (<~9.0)[55] are labeled in the Figure. The acidic pH range where slag dissolution becomes substantial is also labeled, based on refs 52 and 63.

Supporting Information). The solution pH for the samples exposed to 1, 5, and 10 wt % Na_2SO_4 is maintained at ~12.6–12.7, which is similar to that of the Ref–water sample (~12.5). At these pH levels, both the C–(N)–A–S–H gel and hydrotalcite-like phase are stable according to refs 55–58. As a result, Ca and Al in the main binder phases are not readily accessible to SO_4^{2-} ions and hence the extent of gel decalcification and ettringite formation is rather limited.[17,30] This behavior is very different from OPC-based systems undergoing Na_2SO_4 attack, where there are readily available sources of Ca (i.e., portlandite) and Al (i.e., monosulfoaluminate), and, as a result, ettringite and/or gypsum can form extensively, leading to a buildup of crystallization pressure and ultimately cracking and failure of the system.[10–16]

Conversely, for the samples exposed to $MgSO_4$ solutions the pH equilibrates to a much lower level than the samples exposed to Na_2SO_4 solutions. At 1 wt % $MgSO_4$, the pH of the solution is maintained at ~11.9 after 10 days of exposure, and therefore both the C–(N)–A–S–H gel and the hydrotalcite-like phase are still stable, though the conditions are favorable for ettringite formation. However, as the concentration of $MgSO_4$ increases to 5 and 10 wt %, the pH values of the samples drop to ~9.2 and ~8.7, respectively. At these pH levels, the C–(N)–A–S–H gel is no longer stable,[56] which explains the disappearance of the corresponding peaks in these two samples (Figure 1b). According to solubility data of synthetic C–S–H gels, the equilibrium pH of C–S–H gels drop as the Ca/Si ratio of the gel decreases, with a pH value of 8.7–9.2 corresponding to a Ca/Si ratio of 0.[59] This indicates that the C–(N)–A–S–H gel in these two samples is close to full decalcification, with the released Ca^{2+} ions combining with SO_4^{2-} and water molecules to form gypsum. Moreover, the formation of gypsum instead of ettringite in the 5–10 wt % $MgSO_4$-exposed samples is because ettringite is unstable at a pH below ~10.7.[60] Finally, the pH level of 8.7–9.2 aligns well with the equilibrium pH (~8.9) of synthetic M–S–H gels with Mg/Si ratios close to ~1.0.[51] These pH data provide additional, yet indirect, evidence for the transformation of C–(N)–A–S–H to a M–(A)–S–H-type gel in the 5–10 wt % $MgSO_4$-exposed samples.

Figure 2 shows that the H_2SO_4-exposed samples equilibrate to even lower pH levels compared with samples exposed to the same concentrations of $MgSO_4$. This could explain the severe impact H_2SO_4 exposure has on the phase composition of the NaOH-activated slag paste as shown in Figure 1c. At 1 wt % H_2SO_4, the pH of the solution is maintained at ~11.5, and therefore the C–(N)–A–S–H gel and the hydrotalcite-like phase are largely stable[55–58] and so is ettringite.[60] Gypsum also forms in this sample (Figure 1c) since this phase starts to precipitate at a pH below ~11.6, according to predictions from chemical equilibria modeling developed for cement/water systems.[61] As the H_2SO_4 concentration increases to 5 wt %, the pH drops to ~7.8, at which point both the binder phases and ettringite are no longer stable. As a result, both the C–(N)–A–S–H gel and the hydrotalcite-like phase in this sample disappear while extensive gypsum formation occurs as shown in Figure 1c. As the H_2SO_4 concentration increases further to 10 wt %, the exposed solution pH drops to ~1.8, at which all the phases in the paste, including the unreacted slag, are unstable. This explains the disappearance of the broad diffuse peak (attributed to unreacted slag) in the 10 wt % H_2SO_4-exposed sample (Figure 1c).

3.2. Impact of Sulfate Attack on Si/Al Polymerization.

Having elucidated the impact of sulfate attack on the stability of the different phases in the NaOH-activated slag paste, this section examines how the different forms of sulfate exposure change the relative extent of Si/Al polymerization of the main binder phase (i.e., C–(N)–A–S–H gel). This is achieved by evaluating the peak position of the main asymmetric Si–O–T (T = Si or Al) stretching band (mainly attributed to the C–(N)–A–S–H gel) in the FTIR spectrum, which reflects the extent of Si/Al polymerization, with a larger wavenumber generally associated with a higher degree of Si/Al polymerization.[51,56,64] Figure 3a-c shows the FTIR spectra from 500 to 1250 cm^{-1} for the NaOH-activated slag paste exposed to different concentrations of Na_2SO_4, $MgSO_4$ and H_2SO_4 solutions, respectively, with the full FTIR spectra (500–4000 cm^{-1}) given in Figure S3a-c in the Supporting Information. In the FTIR spectra of the 5–10 wt % $MgSO_4$-exposed and 1–10 wt % H_2SO_4-exposed samples, characteristic bands of gypsum (i.e., ~3520, ~3400, ~1680, ~1620, ~1110, ~666, and ~595 cm^{-1})[65] are observed, whereas characteristic bands of ettringite (i.e., ~3630, ~1100, and ~610 cm^{-1})[66] can be observed in the FTIR spectra of the 1–10 wt % Na_2SO_4, 1 wt % $MgSO_4$, and 1 wt % H_2SO_4 samples. These FTIR results are consistent with the XRD results presented in Figure 1.

Figure 3 clearly shows that each type of sulfate exposure has a distinct impact on the main asymmetric Si–O–T stretching band. It is observed that exposure to Na_2SO_4 solutions, even at high concentrations (i.e., 5–10 wt %), does not cause an obvious shift in this band (Figure 3a). This is expected given that the C–(N)–A–S–H gel phase is found to be stable under Na_2SO_4 attack as outlined in the previous section. However, this band is significantly altered after exposure to high concentrations (i.e., 5–10 wt %) of $MgSO_4$ and H_2SO_4 solutions. For the samples exposed to 5–10 wt % $MgSO_4$, the peak position shifts from ~953 cm^{-1} to ~1000 cm^{-1}, which suggests that the C–(N)–A–S–H gel in these two samples has become more polymerized after interacting with $MgSO_4$. This wavenumber is in agreement with the asymmetric Si–O–Si stretching mode of synthetic M–S–H gels with Mg/Si ratios of 0.8–1.3 (~1000 cm^{-1}),[51] which contains a larger proportion of Q^3 and Q^4 than C–(N)–A–S–H gel (predominantly Q^2).

DOI: 10.1021/acs.jpcc.7b11270
J. Phys. Chem. C 2018, 122, 5992–6004

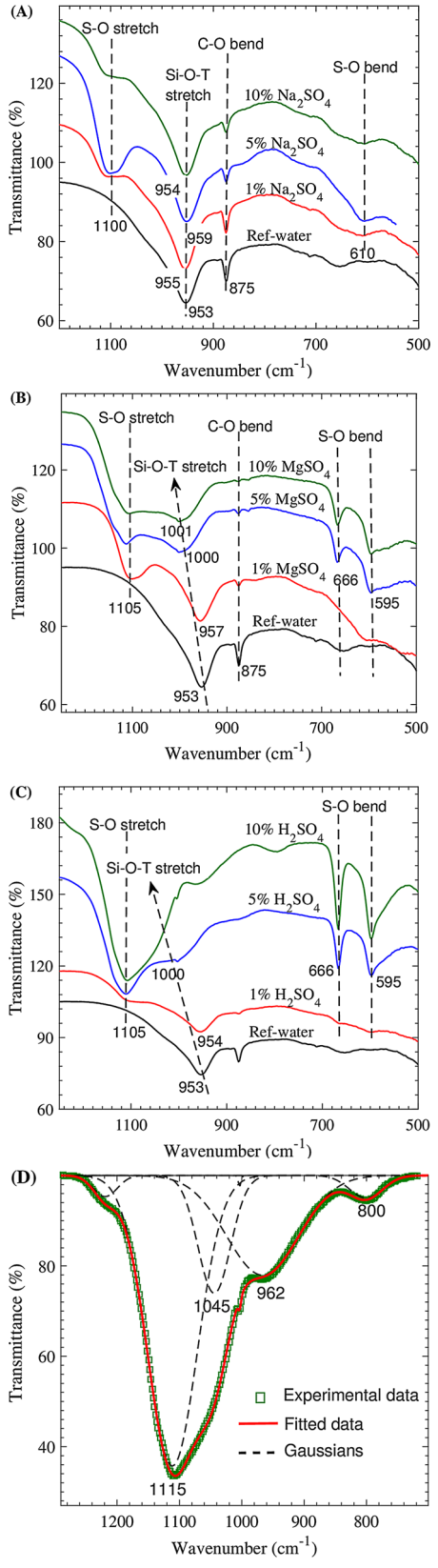

Figure 3. Impact of (a) Na_2SO_4, (b) $MgSO_4$, and (c) H_2SO_4 exposure on the FTIR spectra of NaOH-activated slag paste. (d) Deconvolution of the FTIR spectrum of the sample exposed to 10 wt % H_2SO_4 solution between ~700 and ~1300 cm^{-1} using multiple Gaussians. Note that the data in parts a–c are each given as a stacked plot.

Also, a small shoulder at ~3680 cm^{-1} due to the O–H stretching mode in M–S–H gel[51] can be observed in the two samples exposed to 5–10 wt % $MgSO_4$ (Figure S3b in Supporting Information). These observations provide additional, yet indirect, evidence for the formation of a M–(A)–S–H-type gel phase in the 5–10 wt % $MgSO_4$-exposed samples. The resulting M–(A)–S–H gel is likely to contain a reasonable amount of Al since the solubility of Al at a pH of 8.7–9.2 (equilibration pH values for the 5–10 wt % $MgSO_4$-exposed samples, Figure 2) is relatively low.[67]

H_2SO_4 exposure exhibits an even stronger impact on the asymmetric Si–O–T stretching band compared with $MgSO_4$ as seen in Figure 3c, where this band shifts to overlap with the S–O stretching mode of gypsum (located at ~1115 cm^{-1}) for 10 wt % H_2SO_4. Deconvolution of this peak (Figure 3d) reveals that the main asymmetric Si–O–T stretching band occurs at around ~1045 cm^{-1}, which is close to the corresponding band in silica gel (~1080 cm^{-1}).[68] The mode at ~962 cm^{-1} may be attributed to the Si–O in-plane stretching vibration of Si–OH groups,[69] while the new band at ~800 cm^{-1} can be assigned to Si–O–Si symmetric stretching mode in silica gel.[68] Hence, these data together with the XRD data in Figure S2b (in Supporting Information) reveal that a highly polymerized silica-rich gel with predominantly Q^3 and Q^4 is formed after exposure to 10 wt % H_2SO_4 solution. Because of the relatively high solubility of Al in this sample arising from its low pH (~1.8, Figure 2),[67] it is possible Al is absent/deficient in the resulting gel. For the sample exposed to 5 wt % H_2SO_4, however, Al is likely to be present in the resulting gel since Al solubility is close to its lowest point at a pH of ~7.6[67] (equilibration pH for the 5 wt % H_2SO_4 sample, Figure 2). For this sample, the asymmetric Si–O–T stretching band is located at ~1000 cm^{-1}, which is close to the asymmetric Si–O–T stretching mode in a N–A–S–(H) gel (~1020 cm^{-1}).[56] Hence, an aluminosilicate-type gel is likely to have formed in the 5 wt % H_2SO_4-exposed sample.

The relationship between the equilibrated pH of the sulfate solution and the main asymmetric Si–O–T stretching band of the sulfate-attacked NaOH-activated slag pastes is plotted in Figure 4, which shows that the equilibrated pH of the sulfate solution is inversely related to the location (in cm^{-1}) of the main asymmetric Si–O–T stretching band of the exposed paste. It is clear that a lower equilibrated pH generally leads to a larger wavenumber for this band and hence a higher degree of Si/Al polymerization for the attacked paste. This result suggests

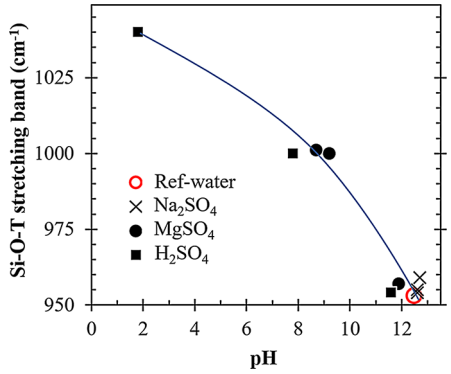

Figure 4. Correlation between the equilibrated pH of the sulfate solution and the peak position of the main asymmetric Si–O–T band of the exposed binder gel. The solid line is provided to guide the eye.

DOI: 10.1021/acs.jpcc.7b11270
J. Phys. Chem. C 2018, 122, 5992–6004

that the extent of Si/Al polymerization for the sulfate-attacked paste is largely controlled by the equilibrated pH of the sulfate solution, which is then related to the type and concentration of the sulfate-bearing solution.

3.3. Impact of Sulfate Attack on the Local Atomic Structure. X-ray PDF analysis is employed to further elucidate how the local atomic structure of the NaOH-activated slag paste is altered by the different forms of sulfate attack. The X-ray PDF results are presented in Figure 5, where the peaks below ~4 Å (the nearest and second nearest neighbor bonding environments) have been assigned based on ref 26 and the simulated X-ray PDFs of ettringite and gypsum (Figure S4 in the Supporting Information). The atom−atom correlations for ettringite and gypsum are labeled in blue and gray text, respectively, in Figure 5. It should be noted that the first peak shown at ~1.2 Å along with any peaks located below ~1.0 Å arise from artifacts generated due to imperfect corrections, termination ripples and statistical noise.[48] The results show that exposure to Na_2SO_4 solutions does not significantly alter the local atom−atom correlations of the NaOH-activated slag paste whereas exposure to $MgSO_4$ and H_2SO_4 solutions, especially at higher concentrations (i.e., 5−10 wt %), results in dramatic changes in the local atom−atom correlations. These dramatic changes are attributed to gypsum precipitation and severe damage to the main binder phase (i.e., C−(N)−A−S−H gel) in these samples. The significant shift of the Si/Al−O peak from ~1.64 Å to ~1.50 Å in Figure 5b,c is caused by the S−O correlation in gypsum located at ~1.43 Å, which suggests that gypsum contributes significantly to the local atom−atom correlations of these four samples (5−10 wt % $MgSO_4$ and H_2SO_4-exposed samples).

Hence, in order to assess the impact of $MgSO_4$ and H_2SO_4 exposure on the local atomic structure of the binder phase (i.e., C−(N)−A−S−H gel), it is necessary to remove the PDF contributions of gypsum from these samples (i.e., 5−10% $MgSO_4$ and H_2SO_4-exposed samples). This has been carried out following the method presented in ref 70. For more details on the removal process and the resulting data quality, refer to ref 70 along with Figure S5 and Table S2 in the Supporting Information. It would be ideal to also remove contributions from ettringite and/or gypsum in the 1, 5, and 10 wt % Na_2SO_4, 1 wt % $MgSO_4$, and 1 wt % H_2SO_4-exposed samples, however, this is extremely difficult if not impossible using the current method,[70] largely due to the relatively small quantities of ettringite and gypsum formed in these samples (no obvious increase in the long-range ordering of the PDF for these samples, see Figure S1 in the Supporting Information).

The short-range ordering in the X-ray PDFs of the $MgSO_4$- and H_2SO_4-exposed AAS pastes after removal of the gypsum contributions from the 5 and 10 wt % samples are shown in Figure 6, parts a and b, respectively. It is seen in Figure 6a that all the samples exposed to $MgSO_4$ exhibit reduced Ca−O and Ca−Si/Al peak intensities compared with the Ref−water sample, which is direct evidence of C−(N)−A−S−H gel decalcification in these samples. As the $MgSO_4$ concentration increases from 1 to 5 wt %, the degree of decalcification increases significantly, however, no further increase occurs as the concentration is raised from 5 to 10 wt %. In fact, the short-range atom−atom correlations for the 5 and 10 wt % $MgSO_4$-exposed samples are almost identical, and the relative amount of gypsum formed in these two samples is essentially the same (as shown in Figure 7a). This is consistent with FTIR results which show that the main asymmetric Si−O−T stretching band

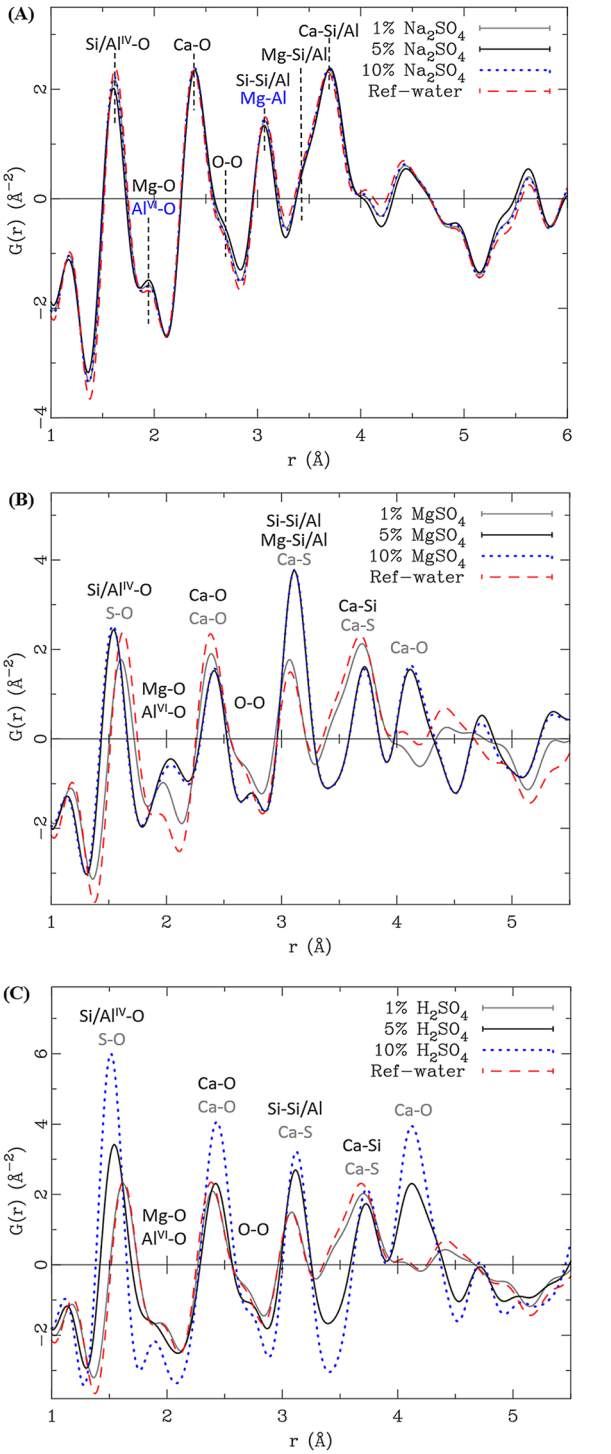

Figure 5. X-ray PDFs showing the impact of exposure to (a) Na_2SO_4, (b) $MgSO_4$, and (c) H_2SO_4 solutions on the local atomic structure of the NaOH-activated slag paste. The atom−atom correlations of ettringite and gypsum are labeled in blue and gray, respectively.

of the 5 and 10 wt % samples are almost identical. These results indicate that decalcification of the C−(N)−A−S−H gel is essentially complete after immersion in a 5 wt % $MgSO_4$ solution for 10 days, and a higher concentration does not induce any additional changes in the local atomic structure of the C−(N)−A−S−H gel nor does it alter the amount of gypsum that precipitates. These results also suggest that the remaining Ca−O and Ca−Si/Al correlations in the 5−10 wt %

DOI: 10.1021/acs.jpcc.7b11270
J. Phys. Chem. C 2018, 122, 5992−6004

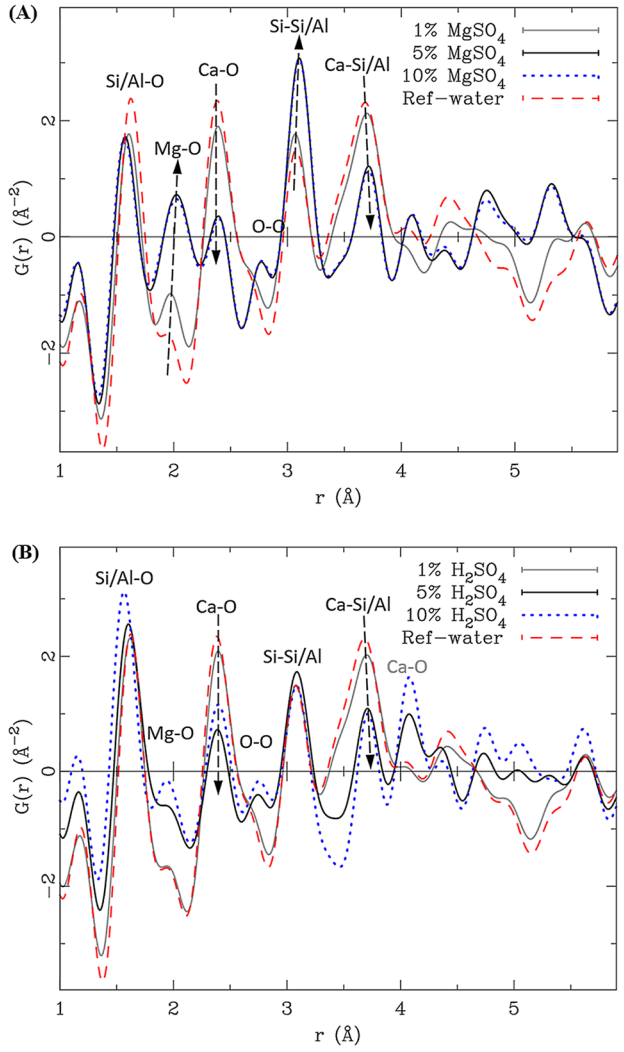

Figure 6. Short-range X-ray PDF data of the samples exposed to (a) $MgSO_4$ and (b) H_2SO_4 solutions after removal of gypsum.

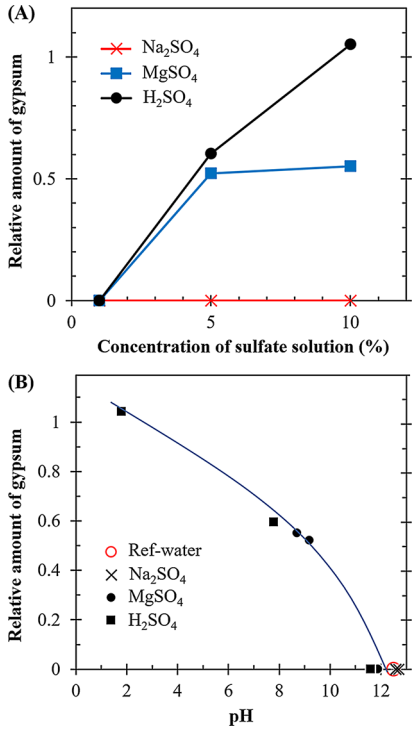

Figure 7. Correlation between the relative amount of gypsum in the paste and (a) the concentration of sulfate solutions and (b) the equilibrated pH of the samples. The solid line in part b is provided to guide the eye.

$MgSO_4$-exposed samples are mainly attributed to the unreacted slag, although there may be a small amount of gypsum still present in Figure 6a due to the imperfect removal of this phase from the PDF data.

Along with the decalcification of the C−(N)−A−S−H gel, the Mg−O/Al^{VI}−O peak intensity is found to increase significantly with increasing $MgSO_4$ concentration (Figure 6a), showing that a considerable amount of Mg has been incorporated into the sample. The loss of Ca and incorporation of Mg suggests that a magnesium/silicate-rich phase is formed via exposure to 5−10 wt % $MgSO_4$. It is observed in Figure 6a that the Si−Si/Al peak intensity is significantly higher for the 5−10 wt % $MgSO_4$-exposed samples than the Ref−water sample. Since the Si−Si/Al correlation reflects the Si/Al tetrahedra connectivity (gel polymerization) to a certain extent,[26] the marked increase in the Si−Si/Al peak intensity with increasing $MgSO_4$ concentration indicates that the resulting gel has a higher degree of polymerization, in agreement with the FTIR results in Figure 3b. Given that there is a substantial amount of Q^3 and Q^4 in M−S−H gel,[51] these results definitively show that a M−(A)−S−H-type gel forms due to $MgSO_4$ attack. As mentioned in the previous section, Al is likely to remain in the gel due to its relatively low solubility at the pH of ∼8.7−9.2, although it is also possible for Al to end up in an amorphous $Al(OH)_3$ gel as has been predicted to occur in highly carbonated OPC paste.[71]

H_2SO_4 exposure is also seen to be destructive to the local atomic structure of the NaOH-activated slag paste, as depicted in Figure 6b. Samples exposed to H_2SO_4 solutions, especially at high concentrations (i.e., 5, 10 wt %), have a significant decrease in the intensities of the nearest Ca−O (at ∼2.35 Å) and Ca−Si/Al correlations, showing that these two samples have undergone severe decalcification. Nevertheless, the nearest Ca−O (at ∼2.35 Å) and Ca−Si/Al correlations are still evident in the 10 wt % sample, and one would expect them to be lower since the results in the previous sections showed that both the unreacted slag and the C−(N)−A−S−H gel have dissolved in this sample. The residual intensity is likely due to some gypsum remaining in the PDF data that could not be removed using the current method, as seen by the relatively strong Ca−O correlation at ∼4.10 Å (attributed to gypsum) in Figure 6b.

Figure 6b shows that the Si−Si/Al peak intensity is higher for the 5 wt % sample than the 1 wt % sample. This indicates that the Si/Al polymerization of the paste increases as the H_2SO_4 concentration increase to 5 wt %, which is consistent with the FTIR results in Figure 3b. However, as the H_2SO_4 concentration increases from 5 to 10 wt %, the Si−Si/Al peak intensity decreases, which, at first glance, may indicate a reduction in the degree of Si/Al polymerization. This contradicts with the FTIR results in Figure 3b, where the resulting gel in the 10 wt % H_2SO_4-exposed sample is highly polymerized. Since both the solubility of Si and Al increases with increasing acidity,[52,67] it is likely that a substantial amount of Si and Al has dissolved in the 10 wt % H_2SO_4 solution and was washed away during the sample treatment process. This lowers the overall Si+Al content remained in the attacked gel, leading to a lower intensity for the Si−Si/Al correlation.

DOI: 10.1021/acs.jpcc.7b11270
J. Phys. Chem. C 2018, 122, 5992−6004

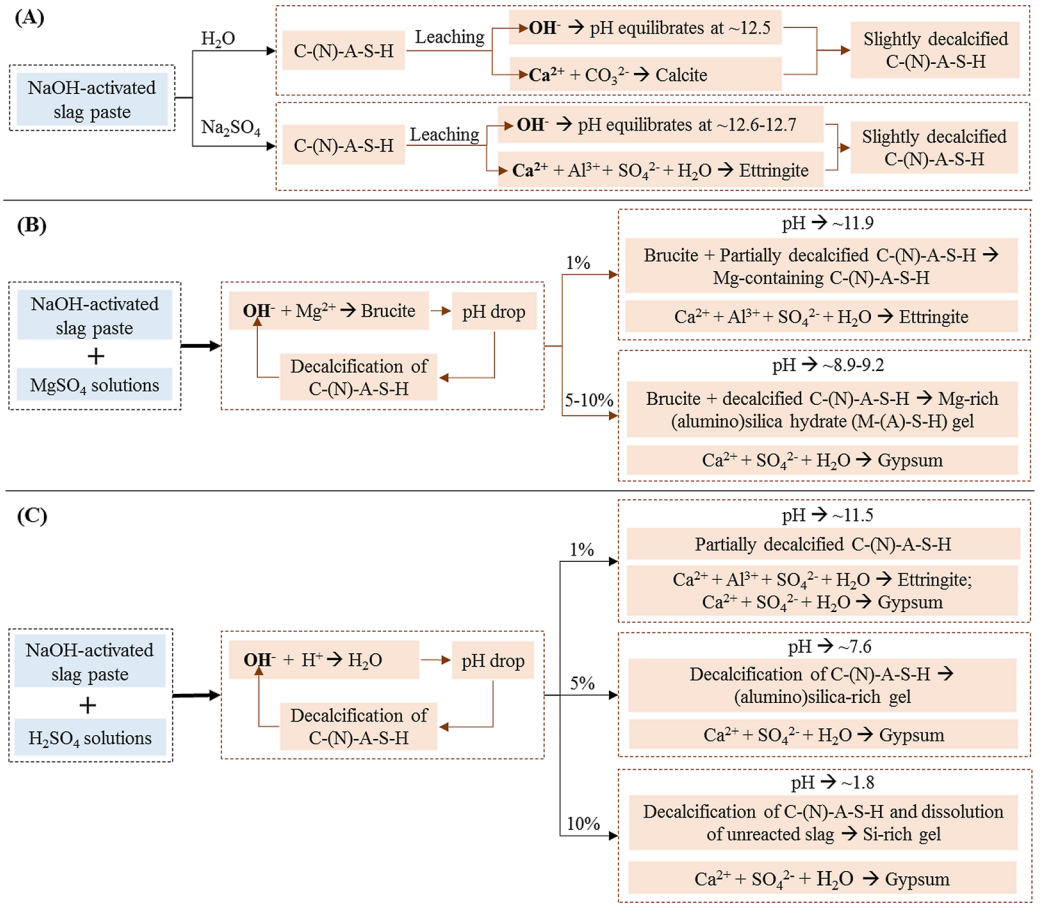

Figure 8. Schematic illustration of the degradation mechanisms for the NaOH-activated slag paste exposed to (a) distilled water and Na_2SO_4, (b) $MgSO_4$, and (c) H_2SO_4 solutions. The sulfate attack mechanism is controlled by the equilibrated pH of the solution, which depends on the type and concentration of the sulfate solution. For $MgSO_4$ attack, the pH is lowered through formation of brucite, which drives decalcification of the C−(N)−A−S−H gel. The decalcified C−(N)−A−S−H gel then combines with brucite to form a Mg-rich (alumino)silica gel, along with precipitation of ettringite or gypsum. For H_2SO_4 attack, the pH is lowered through proton neutralization and excess H^+, which drives dissolution of C−(N)−A−S−H, as well as the unreacted slag in the case of 10 wt % H_2SO_4. In addition to formation of a silica-rich or (alumino)silica-rich gel, ettringite, and/or gypsum precipitates depending on the equilibrated pH levels, similar to the case of $MgSO_4$ attack.

The relative amount of gypsum formed in the different samples was determined by refining the simulated gypsum PDF (Figure S4b in Supporting Information) against the experimental PDF over an r range of 10−50 Å, where the PDF data are dominated by gypsum (refer to Table S2 and Figure S5 in the Supporting Information for more details). The fractional amount of gypsum is plotted against the concentration of the sulfate solutions in Figure 7a, where increasing the $MgSO_4$ concentration from 5 to 10 wt % does not alter the amount of gypsum formed. However, increasing the H_2SO_4 concentration from 5 to 10 wt % almost doubles the amount of gypsum. The additional gypsum in the 10 wt % sample is due to its low equilibrated pH (~1.8, Figure 2) which causes the unreacted slag in the sample to dissolve and supply additional Ca^{2+}. In fact, there is an apparent correlation between the equilibrated pH of the sulfate-attacked sample and the relative amount of gypsum formed, as illustrated in Figure 7b.

3.4. Sulfate Attack Degradation Mechanisms. In the previous sections it was seen that (i) the stability of chemical phases in the NaOH-activated slag paste, (ii) the relative extent of Si/Al polymerization for the C−(N)−A−S−H gel, and (iii) the local atomic structure of the paste are largely controlled by the type and concentration of the accompanying cation (Na^+, Mg^{2+}, or H^+), which, in turn, is linked with the equilibrated pH of the exposed solution. Hence, to elucidate the underlying chemical degradation mechanisms according to the cation type, it is necessary to understand how the different sulfate-bearing chemicals regulate the pH in the pore solution of the samples. This information along with the sulfate attack mechanisms are schematically illustrated in Figure 8.

For samples exposed to distilled water and Na_2SO_4 solutions, the pH is equilibrated via leaching of OH^- from the pore solution to the surrounding immersion solutions (Figure 8a), which is driven by their difference in OH^- concentration. This leaching of OH^- then drives the dissolution of the C−(N)−A−S−H gel to supply OH^- to the pore solution. It is noted that a minor secondary phase calcium hemicarboaluminate hydrate ($C_4Ac_{0.5}H_{12}$) identified in the unexposed sample (Figure S6 in Supporting Information) has not been observed in any of the exposed samples including the Ref−water sample. The dissolution of the $C_4Ac_{0.5}H_{12}$ phase may have also contributed to the supply of OH^- and Ca^{2+} during the different forms of exposure, however, its buffering effect is likely to be limited due to its relatively small quantity. Additional discussion on the $C_4Ac_{0.5}H_{12}$ phase is included in the Supporting Information.

As the concentration of OH^- in the immersion solution increases, the driving force for the leaching of OH^- will diminish quickly since the leached OH^- remains in the

DOI: 10.1021/acs.jpcc.7b11270
J. Phys. Chem. C 2018, 122, 5992−6004

immersion solution. Hence, the pH of these samples, regardless of the concentration of Na_2SO_4 solution studied here, are equilibrated at relatively high levels (~12.6−12.7). At these pH levels, the binder phases (i.e., the C−(N)−A−S−H gel and hydrotalcite-like phase) in the paste are stable according to refs 55−58; hence, the structure of the C−(N)−A−S−H gel (both the degree of Si/Al polymerization (Figure 3a) and the local atomic structure (Figure 5a)) is only slightly altered.

However, the behavior of $MgSO_4$ and H_2SO_4 exposure is very different, where the leached OH^- can be quickly consumed via precipitation of low solubility brucite ($Mg(OH)_2$) or proton neutralization, as illustrated in Figure 8, parts b and c, respectively. These reactions lead to a lower equilibrium pH for the surrounding sulfate solution compared with Na_2SO_4 exposure, which increases the solubility of the C−(N)−A−S−H gel. Any additional OH^- ions liberated from the pore solution or the dissolved binder phases will continue to be taken out of the solution via brucite or H_2O formation, as long as there is abundant supply of Mg^{2+} or H^+ ions remaining in the sulfate solution. As a result, the pH of these systems will equilibrate at much lower levels compared with Na_2SO_4-exposed samples as shown in Figure 2. For samples exposed to a higher concentration of $MgSO_4$ or H_2SO_4 solution, a larger amount of OH^- will be consumed, which, due to the associated drop in solution pH, will increase the solubility of the various phases (i.e., C−(N)−A−S−H and unreacted slag). This explains why the equilibrated pH of the system decreases with increasing concentration of $MgSO_4$ or H_2SO_4 solution (Figure 2), leading to a larger extent of decalcification of the sample. It is also seen from Figure 2 that H_2SO_4 exposure leads to a lower pH value compared with $MgSO_4$ for the same concentration level, which is due to the higher molarity of H_2SO_4 at the same weight percentage and the surplus of H^+ controlling the pH.

Interestingly, the formation of brucite is not detected in any of the $MgSO_4$-exposed samples studied here, similar to several previous studies on $MgSO_4$-exposed AAMs,[17,30] although its formation has been widely reported in OPC-based systems under $MgSO_4$ attack.[12−14,18,31,72,73] It is likely that brucite forms initially in the $MgSO_4$-exposed samples and then reacts with the decalcified C−(N)−A−S−H gel to form a Mg-rich silica gel. A similar reaction pathway (brucite reacting with a silica gel to form a M−S−H gel) has been postulated to occur in OPC-based cement/concrete for advanced stages of $MgSO_4$ attack by a number of studies.[31,73,74] Furthermore, the reaction between brucite and such Al/Si-rich gel has been reported as a common pathway to synthesize M−S−H gel, where mixing MgO and silica fume with water leads to the initial formation of brucite (detected by XRD measurement), which subsequently reacts with silica fume to form M−S−H gel.[51,64,75] The formation of a M−(A)−S−H-type gel in $MgSO_4$-exposed samples is supported by our XRD (Figure S2 in Supporting Information), FTIR (Figure 3b), and PDF results (Figure 6a) as shown in the previous sections.

It is noted that based on the current results we cannot eliminate another possible reaction pathway for the formation of M−(A)−S−H-type gel in the $MgSO_4$-exposed samples, specifically via direct replacement of Ca^{2+} in the C−(N)−A−S−H gel by Mg^{2+}. However, this reaction route needs to be driven by a preferential incorporation of Mg (versus Ca) in the C−(N)−A−S−H gel, which is not supported by the fact that Mg is taken up in a hydrotalcite-like phase (as opposed to ending up in the C−(N)−A−S−H gel) during alkali-activation of slag.[20,24−26] Furthermore, it has been shown recently, via density function theory calculations, that replacement of Ca in a C−S−H structure (14 Å tobermorite) by Mg makes the structure less energetically favorable.[76] Hence, this reaction pathway is less feasible than the first one, where brucite forms initially and then reacts with decalcified C−(N)−A−S−H gel to form M−(A)−S−H gel. Nevertheless, *in situ* data are needed to confirm the reaction pathway, which can be obtained using characterization techniques such as *in situ* X-ray PDF analysis.

Finally, the decalcification of the C−(N)−A−S−H gel also lead to the release of Ca^{2+} and Al^{3+} ions into the solution, which combine with SO_4^{2-} to form ettringite and/or gypsum precipitates (once the saturation point of the specific phase is reached). This formation is linked with the equilibrated pH levels of the solutions together with the pH-dependent solubility of the respective phase as shown in Figure 2 and Figure 8. The degree of Si/Al polymerization and the relative amount of gypsum formed (linked with the extent of decalcification in the sample) are also directly related with the equilibrated pH levels, which then depend on the type and concentration of sulfate solutions, as shown in Figure 4 and Figure 7.

Because of the importance of Mg^{2+} and H^+ in regulating the pH of AAS, it is expected that other types of Mg-containing phases (e.g., $MgCl_2$[77]) or acid (e.g., HCl[9]) could also induce a similar type of decalcification of the cementitious binders/gels. However, the rate of attack by these chemicals could be very different from their sulfate-bearing counterparts, where leached Ca^{2+} can be quickly taken out of the solution via precipitation of gypsum and/or ettringite. This is outside the scope of the current paper, and future research is needed to examine the role played by the different anions (e.g., SO_4^{2-} versus Cl^-).

3.5. Broader Implications. The results presented here reveal that the extent of sulfate attack of a NaOH-activated slag paste is closely linked to the equilibrated pH of the immersed sample, which is then controlled by the type and concentration of the sulfate-bearing chemical. Because of the use of powder samples for immersion, the sulfate attack process has been significantly accelerated, allowing for equilibrium to be reached within a relatively short period for these concentrated sulfate systems. Therefore, quantitative information on the impact of sulfates on the phase stability/deterioration has been obtained quickly and reproducibly. This research has potential implications for the development of testing standards to evaluate sulfate resistance of AAS, which is important for the commercial adoption of AAMs. However, additional research is required to assess the relative speed of the different forms of sulfate attack on powder samples and to evaluate the impact of the transport properties of the samples on the sulfate attack process of AAMs, as well as the connection between the chemical changes/degradation (as observed here) and physical degradation of bulk samples (e.g., expansion, weight loss and loss of strength). Eventually, by combining the sulfate attack results on powder samples (such as the current study) with the transport and physical degradation properties of the solid binder (during sulfate attack), it will be possible in the future to develop mathematical models that predict the service life of AAS-based structures exposed to sulfate-bearing environments. Further research is also required to evaluate the impact of sulfates on the permeability (and pore structure) of the binder.

DOI: 10.1021/acs.jpcc.7b11270
J. Phys. Chem. C 2018, 122, 5992−6004

4. CONCLUSIONS

In this study, we investigated the impact of sulfate attack on the phase stability, relative degree of Si/Al polymerization and local atomic structure of a NaOH-activated slag by using X-ray diffraction (XRD), Fourier transform infrared (FTIR) spectroscopy and X-ray pair distribution function (PDF) analysis. For all concentrations of Na_2SO_4 (1−10 wt %) and low concentrations of $MgSO_4$ and H_2SO_4 (1 wt %), relatively small changes are seen to occur in the paste, in agreement with existing literature, with minimal formation of ettringite and gypsum. This is attributed to the relatively high pH levels (~11.5−12.7) existing in these samples (paste immersed in sulfate solution) caused by slight leaching of OH^- ions from the pore solution of the paste. At higher $MgSO_4$ and H_2SO_4 concentrations there is sufficient Mg^{2+} or H^+ ions in the sample to react with the leached OH^- units causing a drop in the overall pH. For the case of $MgSO_4$, we propose that low solubility brucite ($Mg(OH)_2$) initially forms, but subsequently reacts with the decalcified C−(N)−A−S−H gel to form a M−(A)−S−H-type gel, explaining why no brucite was detected in the experimental results. For concentrated H_2SO_4 solutions (5 and 10 wt %), the pH drops to even lower levels due to the stronger neutralizing effect of H^+, resulting in complete destruction of the binder phases (and even unreacted slag at the highest concentration studied) and formation of a silica-rich gel for the 10 wt % sample and a (alumino)silica rich gel for the 5 wt % sample. This investigation highlights that the degree of sulfate attack in a NaOH-activated slag paste is closely related to the ability of the ions accompanying SO_4^{2-} to regulate the pH of the pore solution in the paste.

■ ASSOCIATED CONTENT

Supporting Information

The Supporting Information is available free of charge on the ACS Publications website at DOI: 10.1021/acs.jpcc.7b11270.

Long-range X-ray PDF data, magnesium−silicate−hydrate gel and silica gel, solution pH before and after immersion of paste, estimation of the time to reach pH equilibrium during sulfate exposure, FTIR spectroscopy, simulated X-ray PDFs of crystalline phases, gypsum contributions in sulfate-exposed samples, and impact of water immersion on the phases in NaOH-activated slag (PDF)

■ AUTHOR INFORMATION

Corresponding Author

*(C.E.W.) Telephone: +1 609 258 6263. Fax: +1 609 258 2799. E-mail: whitece@princeton.edu.

ORCID

Kai Gong: 0000-0002-5884-4607

Notes

The authors declare no competing financial interest.

■ ACKNOWLEDGMENTS

This work was supported by the National Science Foundation under Grant No. 1362039. The authors would like to acknowledge the use of the 11-ID-B beamline at the Advanced Photon Source, an Office of Science User Facility operated for the U.S. DOE Office of Science by Argonne National Laboratory, under U.S. DOE Contract No. DE-AC02-06CH11357. The authors also acknowledge the beamline staff Mr. Kevin Beyer and Dr. Olaf Borkiewicz for their assistance and guidance. The authors would like to thank Prof. Andrew B. Bocarsly for providing access to the FTIR instrument in the Frick Chemistry Laboratory at Princeton University, Dr. Nishant Garg and Mr. Eric McCaslin for their assistance during the synchrotron experiment, and Ms. Maya Ravichandran and Mr. Kengran Yang for their assistance with sample preparation.

■ REFERENCES

(1) Worrell, E.; Price, L.; Martin, N.; Hendriks, C.; Meida, L. O. Carbon dioxide emissions from the global cement industry. *Annu. Rev. Energy Env.* **2001**, *26*, 303−329.

(2) Provis, J. L.; Bernal, S. A. Geopolymers and related alkali-activated materials. *Annu. Rev. Mater. Res.* **2014**, *44*, 299−327.

(3) Monteiro, P. J. M.; Miller, S. A.; Horvath, A. Towards sustainable concrete. *Nat. Mater.* **2017**, *16*, 698−699.

(4) Bullard, J. W.; Jennings, H. M.; Livingston, R. A.; Nonat, A.; Scherer, G. W.; Schweitzer, J. S.; Scrivener, K. L.; Thomas, J. J. Mechanisms of cement hydration. *Cem. Concr. Res.* **2011**, *41*, 1208−1223.

(5) Thomas, J. J.; Jennings, H. M.; Chen, J. J. Influence of nucleation seeding on the hydration mechanisms of tricalcium silicate and cement. *J. Phys. Chem. C* **2009**, *113*, 4327−4334.

(6) Komljenović, M. Mechanical strength and Young's modulus of alkali-activated cement-based binders. In *Handbook of alkali-activated cements, mortars, and concretes*; Pacheco-Torgal, F., Labrincha, J. A., Leonelli, C., Palomo, A., Chindaprasirt, P., Eds.; Woodhead Publishing: Cambridge, U.K., 2015; pp 171−217.

(7) Bernal, S. A.; Provis, J. L. Durability of alkali-activated materials: Progress and perspectives. *J. Am. Ceram. Soc.* **2014**, *97*, 997−1008.

(8) Baščarević, Z. The resistance of alkali-activated cement-based binders to chemical attack. In *Handbook of alkali-activated cements, mortars and concretes*, Pacheco-Torgal, F., Labrincha, J. A., Leonelli, C., Palomo, A., Chindaprasirt, P., Eds.; Woodhead Publishing: Cambridge, U.K., 2015; pp 373−396.

(9) Shi, C.; Roy, D.; Krivenko, P. Durability of alkali-activated cements and concrete. In *Alkali-activated cements and concretes*; Taylor & Francis: Abingdon, U.K., 2006; pp 176−219.

(10) Naik, N. N.; Jupe, A. C.; Stock, S. R.; Wilkinson, A. P.; Lee, P.; Kurtis, K. E. Sulfate attack monitored by microCT and EDXRD: Influence of cement type, water-to-cement ratio, and aggregate. *Cem. Concr. Res.* **2006**, *36*, 144−159.

(11) Monteiro, P. J. M. Scaling and saturation laws for the expansion of concrete exposed to sulfate attack. *Proc. Natl. Acad. Sci. U. S. A.* **2006**, *103*, 11467−11472.

(12) Skalny, J. P.; Marchand, J.; Odler, I. Sulfate attack. In *Sulfate attack on concrete*; Spon Press: London, U.K., 2002; pp 43−126.

(13) Santhanam, M.; Cohen, M. D.; Olek, J. Sulfate attack research - whither now? *Cem. Concr. Res.* **2001**, *31*, 845−851.

(14) Santhanam, M.; Cohen, M. D.; Olek, J. Mechanism of sulfate attack: A fresh look. Part 1: Summary of experimental results. *Cem. Concr. Res.* **2002**, *32*, 915−921.

(15) Yu, C.; Sun, W.; Scrivener, K. Mechanism of expansion of mortars immersed in sodium sulfate solutions. *Cem. Concr. Res.* **2013**, *43*, 105−111.

(16) Müllauer, W.; Beddoe, R. E.; Heinz, D. Sulfate attack expansion mechanisms. *Cem. Concr. Res.* **2013**, *52*, 208−215.

(17) Bakharev, T.; Sanjayan, J. G.; Cheng, Y.-B. Sulfate attack on alkali-activated slag concrete. *Cem. Concr. Res.* **2002**, *32*, 211−216.

(18) Rasheeduzzafar; Al-Amoudi, O. S. B.; Abduljauwad, S. N.; Maslehuddin, M. Magnesium-sodium sulfate attack in plain and blended cements. *J. Mater. Civ. Eng.* **1994**, *6*, 201−222.

(19) Puertas, F.; Palacios, M.; Manzano, H.; Dolado, J. S.; Rico, A.; Rodríguez, J. A model for the C-A-S-H gel formed in alkali-activated slag cements. *J. Eur. Ceram. Soc.* **2011**, *31*, 2043−2056.

(20) Bernal, S. A.; San Nicolas, R.; Myers, R. J.; Mejía de Gutiérrez, R.; Puertas, F.; van Deventer, J. S. J.; Provis, J. L. MgO content of slag

DOI: 10.1021/acs.jpcc.7b11270
J. Phys. Chem. C 2018, 122, 5992−6004

controls phase evolution and structural changes induced by accelerated carbonation in alkali-activated binders. *Cem. Concr. Res.* **2014**, *57*, 33−43.
(21) Myers, R. J.; Bernal, S. A.; Gehman, J. D.; van Deventer, J. S. J.; Provis, J. L. The role of Al in cross-linking of alkali-activated slag cements. *J. Am. Ceram. Soc.* **2015**, *98*, 996−1004.
(22) Churakov, S. V.; Labbez, C. Thermodynamics and molecular mechanism of Al incorporation in calcium silicate hydrates. *J. Phys. Chem. C* **2017**, *121*, 4412−4419.
(23) Kumar, A.; Walder, B. J.; Kunhi Mohamed, A.; Hofstetter, A.; Srinivasan, B.; Rossini, A. J.; Scrivener, K.; Emsley, L.; Bowen, P. The atomic-level structure of cementitious calcium silicate hydrate. *J. Phys. Chem. C* **2017**, *121*, 17188−17196.
(24) Escalante-Garcia, J. I.; Fuentes, A. F.; Gorokhovsky, A.; Fraire-Luna, P. E.; Mendoza-Suarez, G. Hydration products and reactivity of blast-furnace slag activated by various alkalis. *J. Am. Ceram. Soc.* **2003**, *86*, 2148−2153.
(25) Ben Haha, M.; Le Saout, G.; Winnefeld, F.; Lothenbach, B. Influence of activator type on hydration kinetics, hydrate assemblage and microstructural development of alkali activated blast-furnace slags. *Cem. Concr. Res.* **2011**, *41*, 301−310.
(26) Gong, K.; White, C. E. Impact of chemical variability of ground granulated blast-furnace slag on the phase formation in alkali-activated slag pastes. *Cem. Concr. Res.* **2016**, *89*, 310−319.
(27) Lloyd, R. R.; Provis, J. L.; van Deventer, J. S. J. Acid resistance of inorganic polymer binders. 1. Corrosion rate. *Mater. Struct.* **2012**, *45*, 1−14.
(28) Aliques-Granero, J.; Tognonvi, T. M.; Tagnit-Hamou, A. Durability test methods and their application to AAMs: Case of sulfuric-acid resistance. *Mater. Struct.* **2017**, *50*, 36−49.
(29) Abora, K.; Beleña, I.; Bernal, S. A.; Dunster, A.; Nixon, P. A.; Provis, J. L.; Tagnit-Hamou, A.; Winnefeld, F. Durability and testing-chemical matrix degradation processes. In *Alkali activated materials: State-of-the-art report*; Provis, J. L., van Deventer, J. S. J., Eds. Springer: Dordrecht, The Netherlands, 2014; pp 177−221.
(30) Ismail, I.; Bernal, S. A.; Provis, J. L.; Hamdan, S.; van Deventer, J. S. J. Microstructural changes in alkali activated fly ash/slag geopolymers with sulfate exposure. *Mater. Struct.* **2013**, *46*, 361−373.
(31) Bonen, D.; Cohen, M. D. Magnesium sulfate attack on Portland cement paste - I. Microstructural analysis. *Cem. Concr. Res.* **1992**, *22*, 169−180.
(32) Allahverdi, A.; Skvara, F. Sulfuric acid attack on hardened paste of geopolymer cements - Part 1. Mechanism of corrosion at relatively high concentrations. *Ceram. Silik* **2005**, *49*, 225−229.
(33) Allahverdi, A.; Skvara, F. Sulfuric acid attack on hardened paste of geopolymer cements - Part 2. Corrosion mechanism at mild and relatively low concentrations. *Ceram. Silik* **2006**, *50*, 1−4.
(34) White, C. E.; Provis, J. L.; Llobet, A.; Proffen, T.; van Deventer, J. S. J. Evolution of local structure in geopolymer gels: An *in situ* neutron pair distribution function analysis. *J. Am. Ceram. Soc.* **2011**, *94*, 3532−3539.
(35) White, C. E.; Provis, J. L.; Bloomer, B.; Henson, N. J.; Page, K. *In situ* X-ray pair distribution function analysis of geopolymer gel nanostructure formation kinetics. *Phys. Chem. Chem. Phys.* **2013**, *15*, 8573−8582.
(36) Garg, N.; White, C. E. Mechanism of zinc oxide retardation in alkali-activated materials: An *in situ* X-ray pair distribution function investigation. *J. Mater. Chem. A* **2017**, *5*, 11794−11804.
(37) Morandeau, A. E.; White, C. E. The role of magnesium-stabilized amorphous calcium carbonate in mitigating the extent of carbonation in alkali-activated slag. *Chem. Mater.* **2015**, *27*, 6625−6634.
(38) Morandeau, A. E.; White, C. E. *In situ* X-ray pair distribution function analysis of accelerated carbonation of a synthetic calcium-silicate-hydrate gel. *J. Mater. Chem. A* **2015**, *3*, 8597−8605.
(39) Bell, J. L.; Sarin, P.; Provis, J. L.; Haggerty, R. P.; Driemeyer, P. E.; Chupas, P. J.; van Deventer, J. S. J.; Kriven, W. M. Atomic structure of a cesium aluminosilicate geopolymer: A pair distribution function study. *Chem. Mater.* **2008**, *20*, 4768−4776.
(40) White, C. E. Effects of temperature on the atomic structure of synthetic calcium-silicate-deuterate gels: A neutron pair distribution function investigation. *Cem. Concr. Res.* **2016**, *79*, 93−100.
(41) White, C. E.; Provis, J. L.; Gordon, L. E.; Riley, D. P.; Proffen, T.; van Deventer, J. S. J. Effect of temperature on the local structure of kaolinite intercalated with potassium acetate. *Chem. Mater.* **2011**, *23*, 188−199.
(42) Lei, Y.; Lu, J.; Zhao, H.; Liu, B.; Low, K.-B.; Wu, T.; Libera, J. A.; Greeley, J. P.; Chupas, P. J.; Miller, J. T.; et al. Resolving precursor deligation, surface species evolution, and nanoparticle nucleation during palladium atomic layer deposition. *J. Phys. Chem. C* **2013**, *117*, 11141−11148.
(43) Kim, H.; Nakamura, J.; Shao, H.; Nakamura, Y.; Akiba, E.; Chapman, K. W.; Chupas, P. J.; Proffen, T. Local structural evolution of mechanically alloyed $Mg_{50}Co_{50}$ using atomic pair distribution function analysis. *J. Phys. Chem. C* **2011**, *115*, 7723−7728.
(44) Kalkan, B.; Dias, R. P.; Yoo, C.-S.; Clark, S. M.; Sen, S. Polyamorphism and pressure-induced metallization at the rigidity percolation threshold in densified $GeSe_4$ glass. *J. Phys. Chem. C* **2014**, *118*, 5110−5121.
(45) Chupas, P. J.; Chapman, K. W.; Lee, P. L. Applications of an amorphous silicon-based area detector for high-resolution, high-sensitivity and fast time-resolved pair distribution function measurements. *J. Appl. Crystallogr.* **2007**, *40*, 463−470.
(46) Hammersley, A. P.; Svensson, S. O.; Hanfland, M.; Fitch, A. N.; Hausermann, D. Two-dimensional detector software: from real detector to idealised image or two-theta scan. *High Pressure Res.* **1996**, *14*, 235−248.
(47) Hammersley, A. P. *FIT2D: An introduction and overview*. European synchrotron radiation facility internal report ESRF97-HA02T; European Synchrotron Radiation Facility: Grenoble, France, 1997.
(48) Egami, T.; Billinge, S. J. L. *Underneath the Bragg peaks: Structural analysis of complex materials*; Pergamon: Elmsford, NY, 2003.
(49) Qiu, X.; Thompson, J. W.; Billinge, S. J. L. PDFgetX2: A GUI-driven program to obtain the pair distribution function from X-ray powder diffraction data. *J. Appl. Crystallogr.* **2004**, *37*, 678−678.
(50) Farrow, C. L.; Juhas, P.; Liu, J. W.; Bryndin, D.; Božin, E. S.; Bloch, J.; Proffen, T.; Billinge, S. J. L. PDFfit2 and PDFgui: Computer programs for studying nanostructure in crystals. *J. Phys.: Condens. Matter* **2007**, *19*, 335219.
(51) Nied, D.; Enemark-Rasmussen, K.; L'Hopital, E.; Skibsted, J.; Lothenbach, B. Properties of magnesium silicate hydrates (M-S-H). *Cem. Concr. Res.* **2016**, *79*, 323−332.
(52) Garcia-Lodeiro, I.; Palomo, A.; Fernández-Jiménez, A. Crucial insights on the mix design of alkali-activated cement-based binders. In *Handbook of alkali-activated cements, mortars and concretes*, Pacheco-Torgal, F., Labrincha, J. A., Leonelli, C., Palomo, A., Chindaprasirt, P., Eds.; Woodhead Publishing: Cambridge, U.K., 2015; pp 49−73.
(53) Park, H. K.; Bae, M. W.; Nam, I. H.; Kim, S.-G. Acid leaching of $CaO\text{-}SiO_2$ resources. *J. Ind. Eng. Chem.* **2013**, *19*, 633−639.
(54) Yu, M.; Lin, J.; Fang, J. Silica spheres coated with YVO_4:Eu^{3+} layers via sol-gel process: A simple method to obtain spherical core-shell phosphors. *Chem. Mater.* **2005**, *17*, 1783−1791.
(55) Jobbágy, M.; Regazzoni, A. E. Dissolution of nano-size Mg-Al-Cl hydrotalcite in aqueous media. *Appl. Clay Sci.* **2011**, *51*, 366−369.
(56) Garcia-Lodeiro, I.; Palomo, A.; Fernández-Jiménez, A.; Macphee, D. E. Compatibility studies between N-A-S-H and C-A-S-H gels. Study in the ternary diagram $Na_2O\text{-}CaO\text{-}Al_2O_3\text{-}SiO_2\text{-}H_2O$. *Cem. Concr. Res.* **2011**, *41*, 923−931.
(57) Revertegat, E.; Richet, C.; Gegout, P. Effect of pH on the durability of cement pastes. *Cem. Concr. Res.* **1992**, *22*, 259−272.
(58) Ochs, M.; Mallants, D.; Wang, L. Cementitious materials and their sorption properties. In *Radionuclide and metal sorption on cement and concrete*; Springer International Publishing: Cham, Switzerland, 2016; pp 5−16.
(59) Walker, C. S.; Sutou, S.; Oda, C.; Mihara, M.; Honda, A. Calcium silicate hydrate (C-S-H) gel solubility data and a discrete solid

DOI: 10.1021/acs.jpcc.7b11270
J. Phys. Chem. C 2018, 122, 5992−6004

phase model at 25° C based on two binary non-ideal solid solutions. *Cem. Concr. Res.* **2016**, *79*, 1−30.
(60) Myneni, S. C. B.; Traina, S. J.; Logan, T. J. Ettringite solubility and geochemistry of the $Ca(OH)_2$-$Al_2(SO_4)_3$-H_2O system at 1 atm pressure and 298 K. *Chem. Geol.* **1998**, *148*, 1−19.
(61) Reardon, E. J. An ion interaction model for the determination of chemical equilibria in cement/water systems. *Cem. Concr. Res.* **1990**, *20*, 175−192.
(62) Puertas, F.; Fernández-Jiménez, A.; Blanco-Varela, M. T. Pore solution in alkali-activated slag cement pastes. Relation to the composition and structure of calcium silicate hydrate. *Cem. Concr. Res.* **2004**, *34*, 139−148.
(63) Teir, S.; Eloneva, S.; Fogelholm, C.-J.; Zevenhoven, R. Dissolution of steelmaking slags in acetic acid for precipitated calcium carbonate production. *Energy* **2007**, *32*, 528−539.
(64) Lothenbach, B.; Nied, D.; L'Hôpital, E.; Achiedo, G.; Dauzères, A. Magnesium and calcium silicate hydrates. *Cem. Concr. Res.* **2015**, *77*, 60−68.
(65) Ross, S. D. Sulphates and other oxy-anions of Group VI. In *The infrared spectra of minerals*, Farmer, V. C., Ed. Bartholomew Press: Surrey, U.K., 1974; pp 423−444.
(66) Pajares, I.; Martínez-Ramírez, S.; Blanco-Varela, M. T. Evolution of ettringite in presence of carbonate, and silicate ions. *Cem. Concr. Compos.* **2003**, *25*, 861−865.
(67) Holt, P. K.; Barton, G. W.; Wark, M.; Mitchell, C. A. A quantitative comparison between chemical dosing and electrocoagulation. *Colloids Surf., A* **2002**, *211*, 233−248.
(68) Fidalgo, A.; Ilharco, L. M. The defect structure of sol−gel-derived silica/polytetrahydrofuran hybrid films by FTIR. *J. Non-Cryst. Solids* **2001**, *283*, 144−154.
(69) Al-Oweini, R.; El-Rassy, H. Synthesis and characterization by FTIR spectroscopy of silica aerogels prepared using several $Si(OR)_4$ and $R''Si(OR')_3$ precursors. *J. Mol. Struct.* **2009**, *919*, 140−145.
(70) White, C. E.; Daemen, L. L.; Hartl, M.; Page, K. Intrinsic differences in atomic ordering of calcium (alumino)silicate hydrates in conventional and alkali-activated cements. *Cem. Concr. Res.* **2015**, *67*, 66−73.
(71) Georget, F.; Prévost, J. H.; Vanderbei, R. J. A speciation solver for cement paste modeling and the semismooth Newton method. *Cem. Concr. Res.* **2015**, *68*, 139−147.
(72) Irassar, E. F. Sulfate attack on cementitious materials containing limestone filler - A review. *Cem. Concr. Res.* **2009**, *39*, 241−254.
(73) Baghabra Al-Amoudi, O. S. Attack on plain and blended cements exposed to aggressive sulfate environments. *Cem. Concr. Compos.* **2002**, *24*, 305−316.
(74) Cole, W. F. A crystalline hydrated magnesium silicate formed in the breakdown of a concrete sea-wall. *Nature* **1953**, *171*, 354−355.
(75) Zhang, T.; Cheeseman, C. R.; Vandeperre, L. J. Development of low pH cement systems forming magnesium silicate hydrate (M-S-H). *Cem. Concr. Res.* **2011**, *41*, 439−442.
(76) Özçelik, V. O.; White, C. E. Nanoscale charge-balancing mechanism in alkali-substituted calcium-silicate-hydrate gels. *J. Phys. Chem. Lett.* **2016**, *7*, 5266−5272.
(77) Bernard, E.; Lothenbach, B.; Le Goff, F.; Pochard, I.; Dauzères, A. Effect of magnesium on calcium silicate hydrate (C-S-H). *Cem. Concr. Res.* **2017**, *97*, 61−72.

DOI: 10.1021/acs.jpcc.7b11270
J. Phys. Chem. C 2018, 122, 5992−6004